nature sustainability

Article

https://doi.org/10.1038/s41893-025-01649-y

Adaptive interphase enabled pressure-free all-solid-state lithium metal batteries

Received: 10 January 2024

Accepted: 3 September 2025

Published online: 07 October 2025

Check for updates

Guanjun Cen[1,6], Hailong Yu[1,6], Ruijuan Xiao[1,2], Liubin Ben[3], Ronghan Qiao[4], Jing Zhu[1], Xinxin Zhang[1,2], Gaozhan Liu[4], Kemin Jiang[4], Xiayin Yao[2,4] ✉, Heng Zhang[5] ✉ & Xuejie Huang[1,2,3] ✉

All-solid-state lithium metal (Li°) batteries (ASSLMBs) are a promising next-generation energy storage technology due to their use of non-flammable solid electrolytes for enhanced safety and the potential for higher energy density. However, void formation and evolution at the interface between anode and solid electrolyte remains a major challenge, leading to accelerated performance degradation. Departing from traditional interfacial design strategies, here we introduce dynamically adaptive interphases, formed by controllable migration of pre-installed anions in solid electrolytes, to operate ASSLMBs stably under low external pressure. The interphases adapt to the Li° anode volume changes, maintaining close physical contact between the Li° anode and 'rigid' solid electrolyte under low or zero external pressure. The dynamically adaptive interphase enables Li° full cells to deliver excellent rate performance and 90.7% of capacity retention after 2,400 cycles at a current density of 1.25 mA cm^{-2}. Notably, pouch cells with zero external pressure are assembled with 74.4% of capacity retention after 300 cycles. The present work resolves the critical issue of the continuous solid–solid contact loss between Li° anodes and high-modulus solid electrolytes, advancing the practical deployment of ASSLMBs as high-energy, sustainable electrochemical storage systems.

The integration of renewable energy resources into today's energy supply chains has become essential to reduce the rapid consumption of fossil fuels and build sustainable, environmentally friendly energy networks[1]. High-performance rechargeable batteries, capable of reversibly storing and releasing electric energy, are key to bridging gaps in the efficient utilization of renewable energy resources[2]. Among these, all-solid-state lithium metal (Li°) batteries (ASSLMBs) employing solid-state ionic conductors have emerged as strong sustainable contenders due to their higher energy density and intrinsic safety compared to other existing rechargeable battery technologies[3–6]. Most importantly, ASSLMBs offer enhanced technological and economical sustainability by eliminating flammable organic solvents and employing industrially accessible materials[4,7,8].

However, the generation of voids at the interphase between the anode and solid electrolyte leads to interfacial contact losses, resulting in the inferior electrochemical performance of practical ASSLMBs (<1,000 cycles) compared to prevalent lithium-ion batteries (LIBs)[9–13]. These voids arise from unavoidable initial defects inherited from the lamination and film processing of electrode and solid electrolyte materials[11,14–17]. Pristine voids may further evolve due to parasitic interfacial reactions and inhomogeneous Li^+ stripping flux at the anode–electrolyte interphase[12,18]. The detrimental impact of voids is

[1]Institute of Physics, Chinese Academy of Sciences, Beijing, China. [2]Center of Materials Science and Optoelectronics Engineering, University of Chinese Academy of Sciences, Beijing, China. [3]Songshan Lake Materials Laboratory, Dongguan, China. [4]Ningbo Institute of Materials Technology and Engineering, Chinese Academy of Sciences, Ningbo, China. [5]Key Laboratory of Material Chemistry for Energy Conversion and Storage (Ministry of Education), School of Chemistry and Chemical Engineering, Huazhong University of Science and Technology, Wuhan, China. [6]These authors contributed equally: Guanjun Cen, Hailong Yu. ✉e-mail: yaoxy@nimte.ac.cn; hengzhang2020@hust.edu.cn; xjhuang@iphy.ac.cn

exacerbated by uneven Li° plating and its large volume changes[16,19,20], further worsened by pronounced void evolution under low external stack pressure[21–24].

Extensive work has been performed to address contact losses and alleviate interfacial reactions between the Li° anode and solid electrolytes. Using a lithium alloy with slightly high lithiation potentials (versus Li/Li$^+$: for example, LiIn (refs. 25,26), LiAl (ref. 27), LiSi (refs. 28,29), LiSn (ref. 29)) or inserting interlayers with high lithium diffusion rates (for example, Si (ref. 30), Sn (ref. 31), Sb (ref. 32), Al (refs. 19,33), Au (ref. 34)) can homogenize lithium deposition/dissolution. Introducing an artificial solid electrolyte interphase layer with electronic insulation (for example, Li_3N (ref. 35), LiF (refs. 36,37)) can prevent direct contact and undesirable side reactions between the active Li° anode and solid electrolytes. Yet these methods cannot fundamentally resolve the repeated degradation of the interphase during prolonged cycling and mechanical failure readily occurs due to the large volume expansion and contraction of the Li° anode[19,38]. Therefore, it is urgent to develop an effective strategy to dynamically fill voids and sustain intimate physical contact between the Li° anode and solid electrolyte, enabling long-term cycling of ASSLMBs without requiring high external pressures.

Here we introduce dynamically adaptive interphases (DAIs) utilizing migratable anions pre-installed in solid electrolytes to circumvent anode–electrolyte interfacial issues in ASSLMBs. The DAI is implemented in a LiI-doped sulfide electrolyte (that is, $Li_{3.2}PS_4I_{0.2}$) featuring controlled migration of I$^-$ ions and sufficient Li-ion conductivity. The DAI formed at the interface between anode and solid electrolyte ensures close solid–solid contact during continuous Li stripping and plating, permitting stable ASSLMBs operation under external pressures comparable to LIBs (<1 MPa). Our work opens an avenue to address the well-known dependence of solid-state batteries on high external stack pressure.

Results

Migration of selected negative charges in solid electrolytes

For typical lithium-ion conductive solid electrolytes, the transference number of lithium ions is close to unity, and anionic species are generally considered immobilized at lattice sites[39,40]. In contrast to this conventional wisdom, controllable migration of anionic species in solid electrolytes is a prerequisite for achieving a DAI. We employed bond-valence (BV) simulations to evaluate the energy barriers for the diffusion processes (Fig. 1a) for a vast variety of lithium-containing inorganic materials to identify compounds capable of simultaneously transporting lithium ions and anions[41].

Figure 1b shows the migration energy barriers for both Li$^+$ and anions in Li-containing structures from the inorganic crystal structure database. The calculation details are available in Supplementary Table 1 and Supplementary Fig. 1. Within the same structure, anions with energy barriers comparable to those of Li$^+$ ions are considered a second type of mobile ion. The screening of such dual-ion conductors is based on two criteria: (1) the energy barrier for lithium cations, estimated by the BV method, is lower than 1 eV, ensuring fast Li-ion transport[41], and (2) the ratio of the energy barriers for anions to Li$^+$ cations falls within the range of 0.5 to 1.5. These relative values indicate the coupling mode and the interaction strength between the ions[42]. An energy barrier ratio of 0.5–1.5 indicates that the migration ability of the anions is similar to that of the Li$^+$ ions (that is, DAI region; Fig. 1b). Employing this approach, we can preliminarily locate potential solid electrolytes capable of anion transport.

Considering the stability of the Li_3PS_4–LiI system[43,44] and the reducibility resistance and low electronic–high ionic conductivity of LiI[44], we focus on a LiI-doped sulfide electrolyte (that is, $Li_{3.2}PS_4I_{0.2}$). The diffusion coefficient is estimated from the slope of the mean square displacement (MSD) plots, with a high diffusion coefficient indicating a high diffusion rate of ions: for example, 10^{-6} cm^2 s^{-1} for Li$^+$ ions in $Li_2Zr_2Si_2PO_{12}$ at 600 K (ref. 45) and 10^{-5} cm^2 s^{-1} for Li$^+$ ions in $Li_{10}GeP_2S_{12}$ at 600 K (ref. 46). Figure 1c shows the MSD diagram for Li, P, S and I ions in $Li_{3.2}PS_4I_{0.2}$ at 600 K. The MSD values of Li$^+$ ions are nearly one order of magnitude higher than those of the other species, indicating their superior mobility in $Li_{3.2}PS_4I_{0.2}$ ($D_{Li+} = 1.4 \times 10^{-5}$ cm^2 s^{-1} at 600 K). However, the MSD values of S^{2-} and I$^-$ ions increase markedly with the simulation time, reaching values of 4.7 Å^2 and 8.5 Å^2 at 92 ps, respectively. The respective diffusion coefficients of S^{2-} and I$^-$ ions are estimated to be as high as 8.5×10^{-7} cm^2 s^{-1} and 1.5×10^{-6} cm^2 s^{-1}, suggesting that both S^{2-} and I$^-$ species are mobile under the simulation conditions. The radial distribution functions and coordination numbers of the I–Li and P–S pairs remain almost unchanged, especially in the first peak region, indicating that the structural framework remains stable during simultaneous movement of the Li$^+$ ions and anions (Fig. 1d). Figure 1e,f further compares the possible diffusion pathways of the S^{2-} and I$^-$ ions in $Li_{3.2}PS_4I_{0.2}$. The S^{2-} ions are distributed around the P^{5+} ions and are coupled to the Li$^+$ migration in rotation mode[42,47], with no broken P–S bonds or migration of S^{2-} ions from one $[PS_4]^{3-}$ group. However, the I$^-$ ions readily migrate from one interstitial site to the adjacent gap sites, suggesting that long-range I$^-$ migration through this interstitial mechanism is probably in LiI-doped Li_3PS_4.

Based on the computational results, we synthesized a LiI-doped solid electrolyte (that is, $Li_{3.2}PS_4I_{0.2}$) via simple ball-milling processes. The chemical structures of the as-obtained $Li_{3.2}PS_4I_{0.2}$ were confirmed by X-ray powder diffraction (Supplementary Fig. 2). The total ionic conductivity of $Li_{3.2}PS_4I_{0.2}$ is substantially higher than that of pristine Li_3PS_4 (that is, 2.3 mS cm^{-1} for $Li_{3.2}PS_4I_{0.2}$ versus 0.4 mS cm^{-1} for Li_3PS_4 at room temperature; Supplementary Fig. 3) owing to the presence of a highly conductive phase (that is, thio-LISICON II analogue) in the LiI-doped electrolyte[48,49]. Notably, the Li-ion transference number (T_{Li+}) of $Li_{3.2}PS_4I_{0.2}$ is slightly lower than that of bare Li_3PS_4 (that is, 0.84 for $Li_{3.2}PS_4I_{0.2}$ versus 0.94 for Li_3PS_4; Fig. 1g; see also Supplementary Fig. 3 and Supplementary Table 2), due to the increased mobility of the anionic species in the presence of I$^-$ anion. This corroborates the MD simulations, in which I$^-$ ions migrate alongside Li$^+$ cations. The addition of LiI to Li_3PS_4 endows the corresponding solid electrolyte with controllable anionic conductivity, fulfilling the requirements for DAI formation.

Interestingly, an extremely low fraction (that is, $Li_{3+x}PS_4I_x$, $x < 0.05$) of LiI may result in insufficient iodide anion transport to match interfacial processes (Supplementary Fig. 4), impeding DAI formation kinetics at the anode surface. Conversely, an excessive amount of iodide (that is, $Li_{3+x}PS_4I_x$, $x > 0.5$) causes a marked drop in ionic conductivity, introducing additional factors that may mask the unique impact of the DAI. Hence, an optimal LiI stoichiometric fraction of 0.2 was selected to validate the DAI concept in the following sections.

Building up DAIs

To verify the possibility of building DAIs by introducing selected anions into solid electrolytes, prototype symmetric cells comprising either $Li_{3.2}PS_4I_{0.2}$ or Li_3PS_4 as the solid electrolyte and a lithium–boron (Li–B) alloy as the electrode were assembled and characterized (Fig. 2). The Li–B alloy, composed of a mixture of free metallic lithium and alloy phase[50,51] (that is, mainly Li_5B_4), is utilized as the electrode owing to its similar electrochemical behaviour but higher modulus compared to Li° electrodes, enabling clear observation of the anode–electrolyte interphases at the microscopic level (Supplementary Discussion 1). After storage at 80 °C for 200 h, the $Li_{3.2}PS_4I_{0.2}$ electrolyte still exhibits a relatively uniform distribution of S, P and I elements without discernible iodide accumulation (Supplementary Fig. 5), implying that $Li_{3.2}PS_4I_{0.2}$ is chemically stable and that thermal diffusion is unlikely during the storage period. With continuous Li stripping (100 h), micron-sized voids form at the interphases, accompanied by a detrimental loss of physical contact between the Li–B alloy and Li_3PS_4 electrolyte (Fig. 2b). For the LiI-doped electrolyte, a thin (~5 µm) LiI layer forms at the interphases under the same test conditions (Fig. 2c). Notably, sulfur- and

https://doi.org/10.1038/s41893-025-01649-y

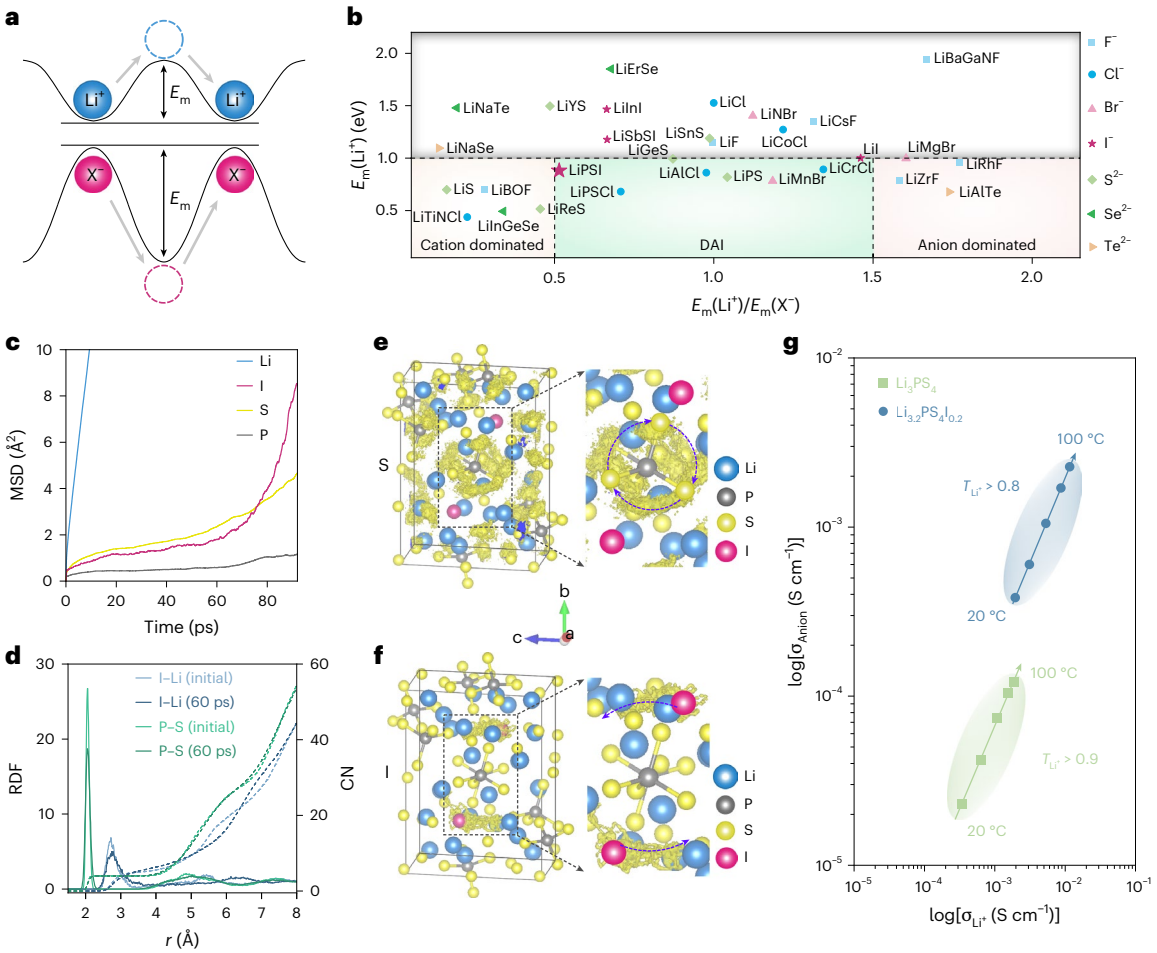

Fig. 1 | First-principles calculations and experimental verification of anion migration in solid electrolytes. a, Schematic illustration of the migration energy barriers (E_m) for cations and anions in solid electrolytes. **b**, Migration energy barriers of some selected anions computed by BV simulations for building DAIs. Detailed information on each anion family is provided in Supplementary Table 1 and Supplementary Fig. 1, in which the exact values for each data point of $E_m(Li^+)/E_m(X^-)$ (abscissa axis) and $E_m(Li^+)$ (ordinate axis) are provided. **c**, MSD plots of Li, I, S and P ions in $Li_{3.2}PS_4I_{0.2}$ obtained by AIMD at 600 K. **d**, Radial distribution functions (RDF) and integrated and coordination numbers (CN) of I–Li and P–S pairs in $Li_{3.2}PS_4I_{0.2}$. **e**,**f**, Trajectories of S (**e**) and I (**f**) ions obtained by AIMD simulations at 600 K. **g**, Ionic conductivities of Li^+ cations and anions in Li_3PS_4 and $Li_{3.2}PS_4I_{0.2}$ electrolytes obtained via electrochemical methods.

phosphorus-containing species are absent in the LiI layer, indicating that the layer is generated via electrochemical processes instead of chemical reactions at the interface.

To verify the chemical composition of the as-formed layer, in situ X-ray photoelectron spectroscopy (XPS) experiments were performed (Fig. 2d,e and Supplementary Fig. 6). The cell, comprising metallic lithium as the counter and reference electrodes and $Li_{3.2}PS_4I_{0.2}$ as the electrolyte, was placed in the XPS chamber[52]. The working electrode was generated via electron beam treatment of the surface of $Li_{3.2}PS_4I_{0.2}$. As shown in Fig. 2e, the characteristic signal of metallic lithium (that is, 52 eV) appears alongside a decrease in the phosphorus signal (that is, 132 eV) assigned to the $Li_{3.2}PS_4I_{0.2}$ electrolyte after electron beam treatment, confirming the successful formation of metallic lithium as the working electrode. During Li stripping processes (driven by low-energy ions; see experimental details[52]), signals of lithium cations (that is, 53 eV) and iodide anions (that is, 631 eV and 619 eV) are observed, whereas phosphorus signals related to the $Li_{3.2}PS_4I_{0.2}$ electrolyte are absent (Fig. 2e). This clearly indicates that LiI is the major species in the interphase layer between Li° anode and solid electrolyte, as observed in the scanning electron microscopy (SEM) experiments. Thus, an effective DAI layer can be built at the Li/$Li_{3.2}PS_4I_{0.2}$ interface through iodide anion migration, ensuring close solid–solid contact between the Li° electrode and solid electrolyte.

DAIs for ASSLMBs

To evaluate the practical suitability of DAIs for improving the electrochemical performance of ASSLMBs, the electrochemical performance of lithium anodes in symmetric (that is, Li°||Li°) and $Li_4Ti_5O_{12}$ (LTO) cells was carefully examined. The protocols for cell assembly are provided in Supplementary Discussion 2. The 'zero strain' electrode material LTO (that is, <1% volume change during charge and discharge cycles[53]) was used as the cathode to minimize issues caused by the cathode–electrolyte interface, such as solid electrolyte losing contact with cathode particles due to volume effect or oxidation decomposition at high potentials[10,54,55]. The DAI approach allows the lithium symmetric cells to work under stringent conditions: for example, a high areal capacity of 5 mAh cm^{-2} and a low external pressure of 0.6 MPa (Supplementary Fig. 7). The electrochemical performance achieved with DAI outperforms those reported in previous works, as compared in Fig. 3a (see detailed data in Supplementary Table 3). Under higher current densities (for example, 2.0 mA cm^{-2}), the DAI-containing cells display improved cycling stability and cycle life compared to reference cells (Supplementary Fig. 8), attributed to the formation of DAIs that dynamically link the solid electrolyte to the electrode surface, eliminating intrinsic or adventitious voids during cycling (Supplementary Fig. 9).

Furthermore, the electrochemical performance of Li–B||LTO cells is provided in Supplementary Fig. 10. In the reference cell,

https://doi.org/10.1038/s41893-025-01649-y

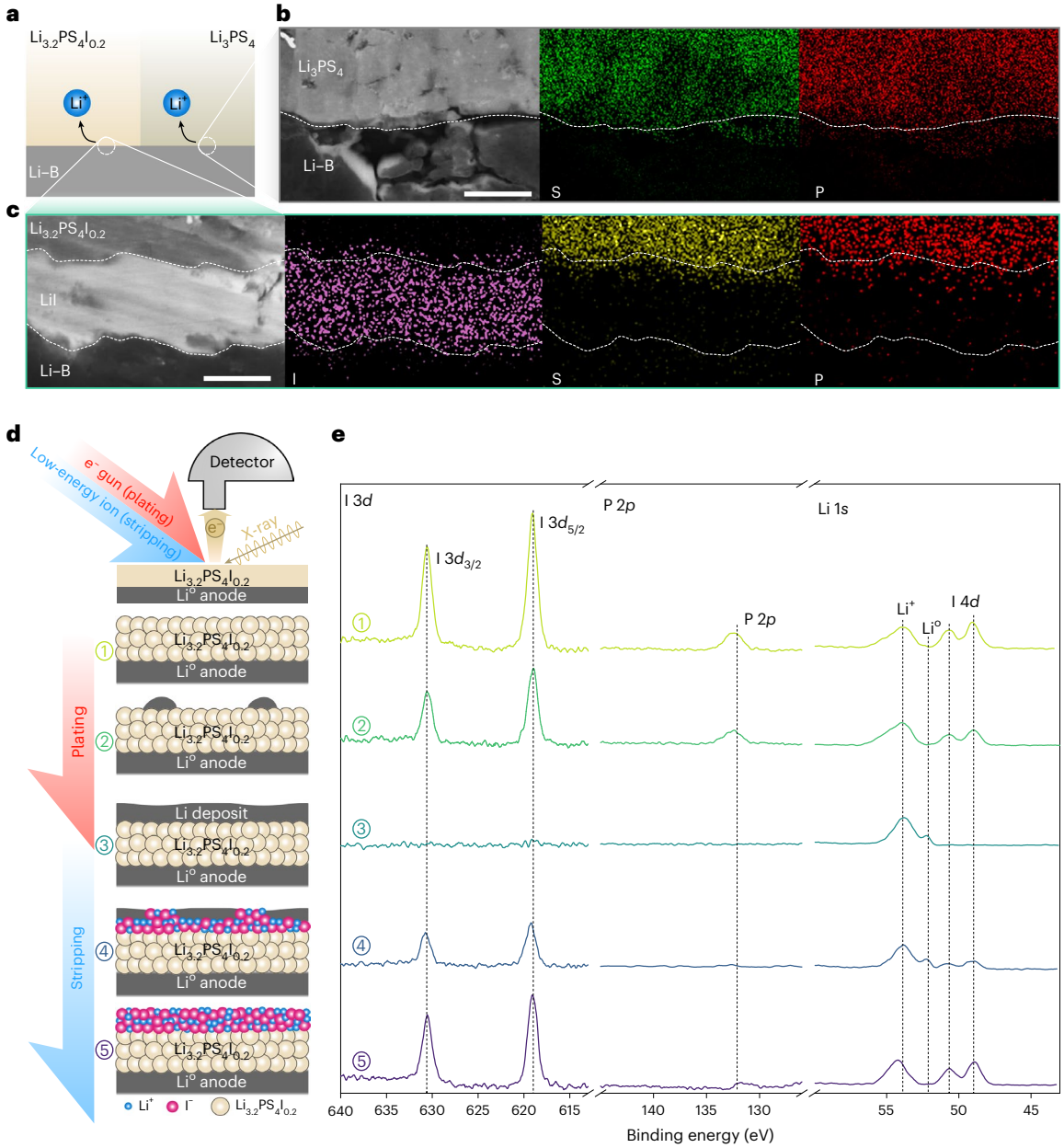

Fig. 2 | Electric field-driven migration of iodide ions to form iodide-rich DAIs. a, Schematic illustration of the symmetric cells with Li_3PS_4 and $Li_{3.2}PS_4I_{0.2}$ electrolytes for studying the morphology between electrode and electrolyte during Li stripping. **b**–**c**, Cross-sectional SEM images and energy-dispersive X-ray spectroscopy mapping of I, S and P for the symmetric cells of Li–B|Li_3PS_4|Li–B (**b**) and Li–B|$Li_{3.2}PS_4I_{0.2}$|Li–B (**c**) cycled at 80 °C. Scale bars, 5 µm. **d**, Schematic illustration of an in situ XPS platform for tracking interfacial composition between Li° anode and electrolyte during Li plating and stripping (see also Methods for experimental details). **e**, Corresponding XPS spectra for I, P and Li under different electrochemical conditions.

the discharge capacity drops rapidly after only ten cycles, accompanied by pronounced cell polarization (Supplementary Fig. 10). This is mainly attributed to the loss of physical contact between the electrolyte and Li° anode, as evidenced by the increased bulk resistance (R_b = 3,536 Ω cm^2 (tenth) versus 138 Ω cm^2 (first); Supplementary Fig. 11). In contrast, introducing lithium iodide to Li_3PS_4 substantially improves cycling stability, owing to markedly suppressed cell polarization (Supplementary Discussion 3). The Li–B|$Li_{3.2}PS_4I_{0.2}$|LTO cell shows an excellent discharge capacity of 75 mAh g^{-1} (Fig. 3b) at a high C-rate of 5 C (1 C = 0.55 mA cm^{-2}), suggesting that the as-formed LiI-based DAI allows rapid Li^+ ion transport across the interphase between the Li–B anode and solid electrolyte. During long-term cycling, the Li–B|$Li_{3.2}PS_4I_{0.2}$|LTO cell shows an extremely high discharge capacity of 113.8 mAh g^{-1} at the 2,400th cycle, corresponding to a superior capacity retention of 90.7% (Fig. 3d). Notably, the charge and discharge curves show only a slightly increase in internal polarization after more than 2,400 cycles (Fig. 3c). Furthermore, increasing the areal loading of the LTO electrode to 2.1 mAh cm^{-2} further improves the cyclic performance of Li–B||LTO cells through the DAI concept, as shown in Supplementary Fig. 12. Benefiting from the universality of DAI, ASSLMBs assembled with high-energy-density positive electrodes such as $LiCoO_2$ and FeS_2 demonstrate promising cycling stability (Supplementary Fig. 13).

To further validate the effectiveness of DAIs under mainstream manufacturing processes in the contemporary battery industry, pouch cells were adopted to replace the above mould cells. Minimal volume expansion at extremely low stack pressure (<5 MPa) could enable pouch cells with higher energy efficiency and reliability at the pack level[56].

https://doi.org/10.1038/s41893-025-01649-y

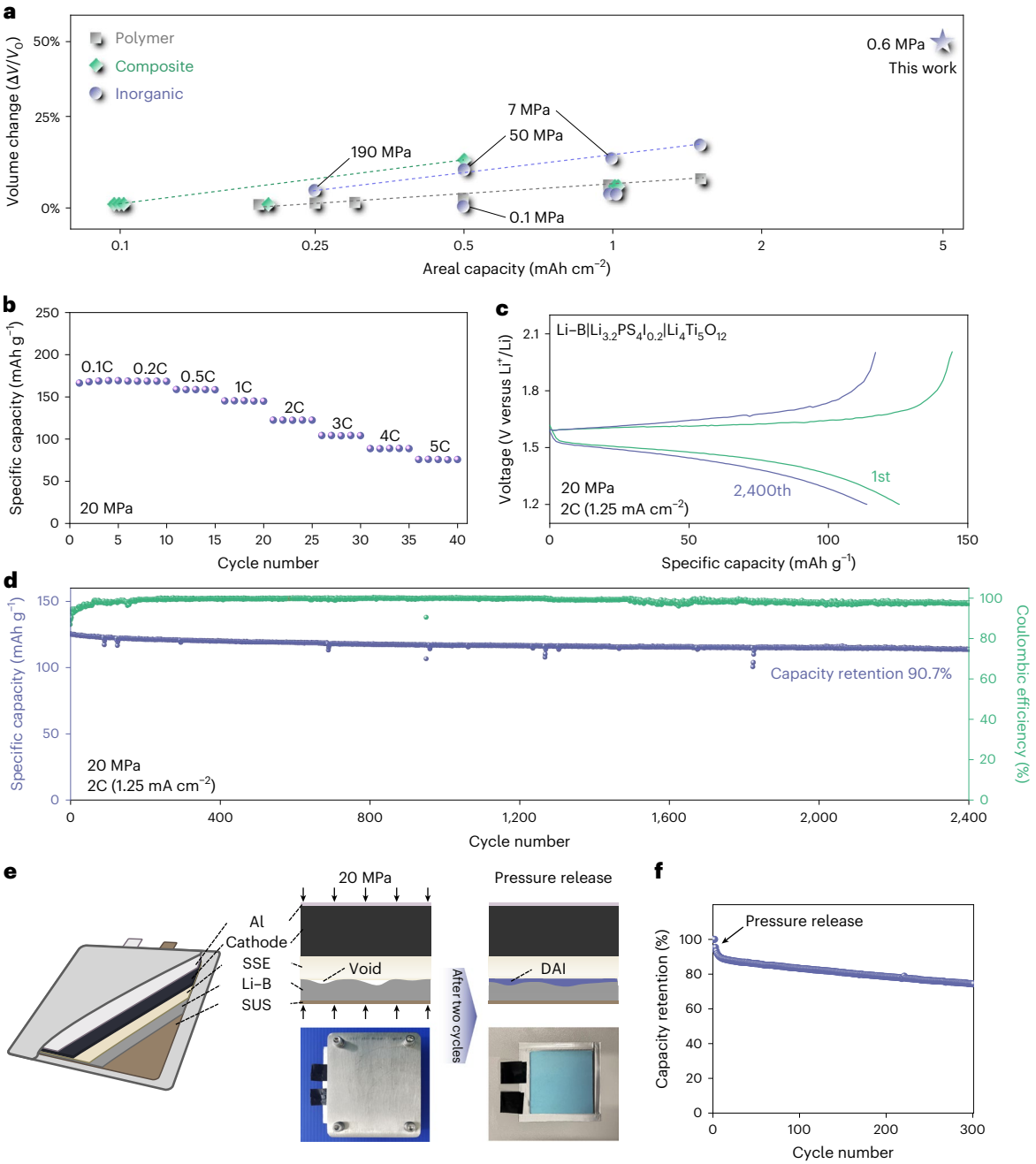

Fig. 3 | DAIs enabling excellent electrochemical cycling performance. **a**, Comparison of the volume changes and capacities of Li metal symmetric cells with different solid electrolytes and external pressures[14,16,44,61–77]; the details are provided in Supplementary Table 3. **b**–**d**, Rate performance (**b**), charge–discharge curves (1st and 2,400th cycles) (**c**) and capacity retention and coulombic efficiency (**d**) of the Li–B|$Li_{3.2}PS_4I_{0.2}$|$Li_4Ti_5O_{12}$ cells. **e**, Sketch and digital photos of the Li–B||$LiCoO_2$ pouch cell: an external pressure of 20 MPa was uniformly applied to the pouch cell for the first two cycles, and the external pressure was removed for the upcoming cycles. SSE, solid-state electrolyte; SUS, Steel Use Stainless. **f**, Cyclic performance of the assembled Li–B||$LiCoO_2$ pouch cell with DAI.

Figure 3e illustrates the configuration and digital photos of the pouch cells (30 mm × 30 mm) assembled in this work, and Fig. 3f displays their capacity retention after various cycles. Initially, the cells were subjected to a stacking pressure of 20 MPa to ensure good physical contact between battery components and uniformly build DAI (Supplementary Discussion 4). As shown in Fig. 3f, nearly 95% of the initial discharge capacity (that is, 96 mAh g^{-1}) is obtained upon the removal of external pressure, possibly due to a lower utilization degree of cathode materials. However, the pouch cell exhibits superior cycling stability (that is, 74.4% capacity retention after 300 cycles) without external pressure. Even at a high areal capacity loading of 2.1 mAh cm^{-2}, the pouch cell demonstrates stable cyclic performance for over 25 cycles (Supplementary Fig. 14).

Mechanistic understanding

To understand the working mechanism of DAIs in ASSLMB cells, further characterizations were performed on the interphases between the Li° anode and solid electrolyte. Figure 4 shows SEM images combined with Auger electron spectroscopy (AES) element mapping of the cycled cells in Supplementary Fig. 10. After cycling, large voids and Li dendrites are observed in the bulk electrolyte of the reference system (that is, Li_3PS_4; Fig. 4b). An enlarged region in Fig. 4c further reveals the presence

https://doi.org/10.1038/s41893-025-01649-y

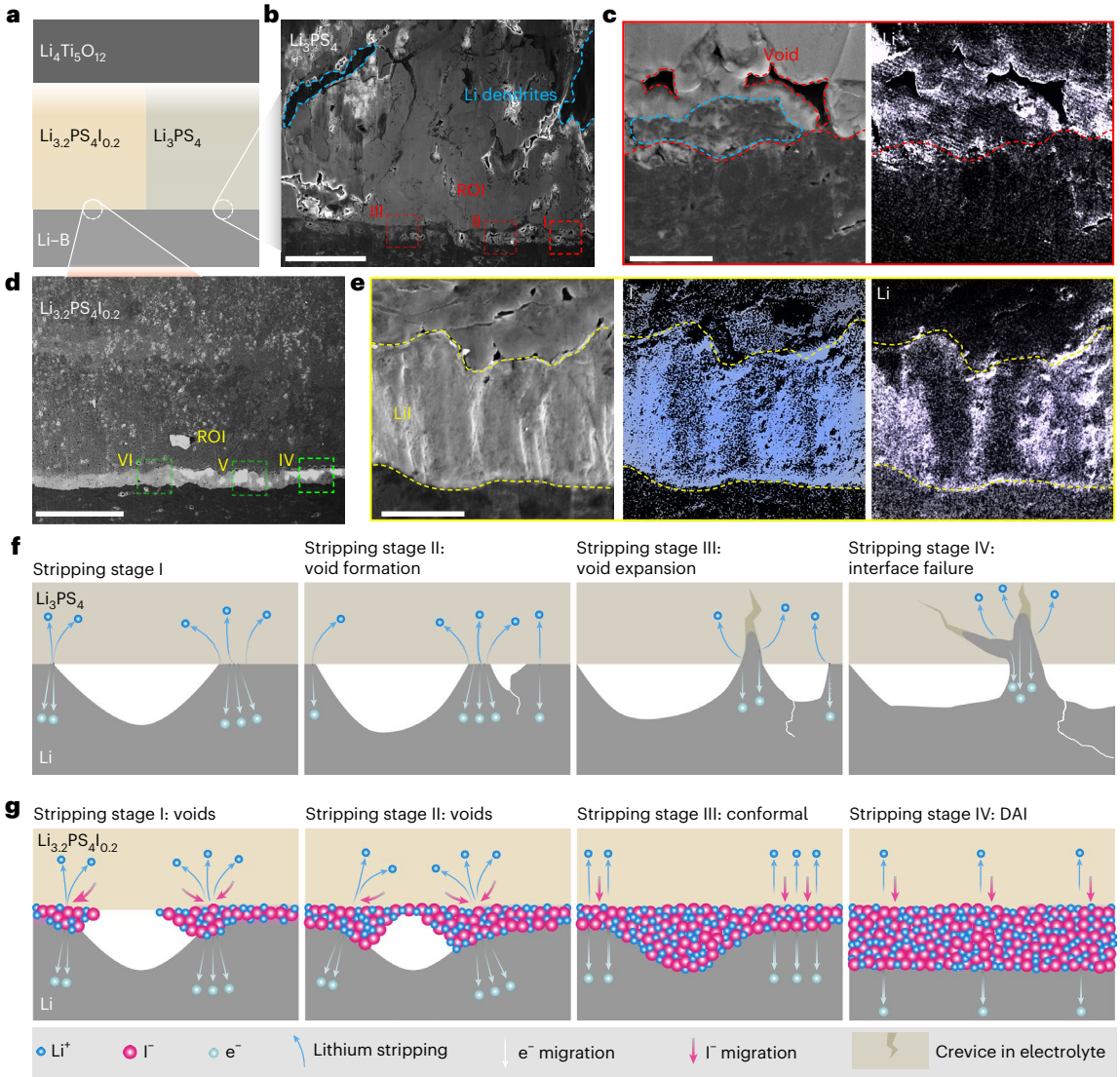

Fig. 4 | Mechanistic understanding on DAI-stabilized ASSLMBs. a, Schematic illustration of symmetric cells with Li_3PS_4 and $Li_{3.2}PS_4I_{0.2}$ electrolytes for studying the interfacial morphology between electrode and electrolyte after cycling. **b**–**c**, Low-magnification cross-sectional SEM image (**b**), and magnified view and AES map (**c**) of the Li-B|Li_3PS_4 interphase in the stripping state. **d**–**e**, Low-magnification cross-sectional SEM image (**d**), and magnified view and AES map (**e**) of the Li-B|$Li_{3.2}PS_4I_{0.2}$ interphase in the stripping state. Scale bars, 50 μm (**b**,**d**) and 10 μm (**c**,**e**). Both cells were subjected to continuous discharge/charge processes for 20 cycles. For the same sample, several regions are randomly selected for zoomed-in views at higher magnifications, and regions I and IV are given in **c** and **e**, respectively. The other regions are presented in Supplementary Fig. 16. **f**,**g**, Working principles of DAI in improving the cyclic performance of ASSLMBs in the stripping state: conventional cells without DAIs (**f**) and cells with DAIs (**g**). More details related to the plating state and subsequent cycles are presented in Supplementary Fig. 30. ROI, region of interest.

of numerous voids at the anode–electrolyte interphases, leading to substantial spatial disconnection between the Li–B anode and Li_3PS_4 electrolyte. These disconnected regions dramatically increase cell resistance, thereby causing deteriorated cyclic performance. Void formation can be attributed to (1) the accumulation of lithium vacancies between the anode and electrolyte during Li stripping and (2) the lower internal creep diffusion rate of the Li° phase compared to the electrochemical stripping rate of Li^+ at the interfaces[15]. In contrast, the $Li_{3.2}PS_4I_{0.2}$-based system shows close physical contact at the anode–electrolyte interfaces, with no voids or Li dendrites observed after cycling (Fig. 4d,e). A LiI-based interphase forms between the Li–B alloy anode and $Li_{3.2}PS_4I_{0.2}$ electrolyte. Enlarged SEM images of the dashed frames (II, III, V and VI) in Fig. 4b,d are provided in Supplementary Figs. 15–17.

To further demonstrate the dynamic evolution of the as-formed DAI, SEM measurements were performed on both electrodes. As seen in Supplementary Fig. 18, LiI-rich DAI form between the electrode (Li–B_1#) and the solid electrolyte under stripping conditions. Simultaneously, iodide signals at the counter electrode (Li–B_2#) show a homogenous distribution without a clear concentration gradient, indicating that LiI-rich DAIs form only at the 'stripping' electrode (Li–B_1#). By reversing the current direction, iodide accumulation is observed at the Li–B_2# electrode (that is, under stripping conditions), indicating the formation of LiI-rich DAIs. Meanwhile, the previously formed LiI-rich DAIs at the Li–B_1# electrode remain nearly unchanged. This clearly suggests that the as-formed LiI-rich DAIs are localized between the electrode and solid electrolyte, as verified by experiments with an iodide-free solid electrolyte (Li_3PS_4) and a LiI-protected lithium electrode (Supplementary Figs. 19–21).

Because the iodide content in the $Li_{3.2}PS_4I_{0.2}$ electrolyte remains mostly unchanged after forming the relatively thin LiI-rich DAIs (that is, shifting from $Li_{3.2}PS_4I_{0.2}$ to $Li_{3.187}PS_4I_{0.187}$; Supplementary Discussion 5), the stabilization of electrode–electrolyte interfaces via the DAI

concept primarily stems from the unique features of DAIs. Notably, the average thickness of the as-formed DAIs is related to the initial interface roughness and the volumetric effects of lithium deposition and stripping during electrochemical cycling (Supplementary Discussion 6) but remains nearly unchanged in sulfide electrolytes with increasing LiI content (Supplementary Fig. 22), applied current density (Supplementary Fig. 9) or cycling time (Supplementary Fig. 23). This suggests that the growth of the as-formed DAIs tends to be self-limited, independent of extrinsic physical and electrochemical parameters.

To better visualize the morphological evolution of DAIs, we employed a surface-textured electrolyte pellet to artificially create repeated voids at the microscale level (Supplementary Discussion 7). Under stripping conditions, LiI-rich DAIs incubate at the junction of the electrode and solid electrolyte, where lithium cations generated by the electrochemical oxidation of the electrode come into contact with iodide anions migrated from the solid electrolyte. With extended stripping time, the three-dimensional percolation of the DAI gradually occupies the artificial voids and rebuilds close physical contact between solid electrolyte and electrode (Supplementary Figs. 24 and 25). Instead of a simple LiI interlayer, the DAIs are probably composed of multiple phases, including a LiI-rich phase (mostly amorphous state; Supplementary Figs. 26 and 27) and two transition phases with either $Li_{3.2}PS_4I_{0.2}$ or the lithium electrode. Within the transition phase between $Li_{3.2}PS_4I_{0.2}$ and the LiI-rich phase, the presence of an iodide gradient brings robust chemical linkages between the DAI and the parent $Li_{3.2}PS_4I_{0.2}$ layer. Similarly, the transition phase between the lithium electrode and the LiI-rich phase reduces the nucleation overpotential for lithium plating (Supplementary Fig. 28) and allows dynamic anchoring of the DAI to the lithium electrode, promoting uniform lithium plating (Supplementary Discussion 8). Consequently, the DAIs tightly link the solid electrolyte to the lithium electrode even under low external pressure (that is, 'octopus-like' behaviour; Supplementary Fig. 29).

Based on the above experimental observations, the working mechanism of DAI in ASSLMBs is illustrated in Fig. 4f,g. Before electrochemical tests, innate voids form at the interface between the Li anode and electrolyte during cell assembly (stage I in Fig. 4f,g) due to unavoidable surface defects in the pristine electrolyte and Li° anode. In conventional cells, these innate voids, combined with new voids formed during stripping (stages II–IV in Fig. 4f), result from the quick depletion of lithium ions at the outer surface of the Li° anode at low external stack pressure. These intrinsic and newly formed voids lead to dendritic lithium deposition and crack formation within the bulk electrolyte during the plating and stripping processes (stages V and VI of Supplementary Fig. 30a), markedly increasing interfacial resistance and internal polarization and ultimately causing cyclic performance to deteriorate[21,22,57]. In contrast, the detrimental impact of voids is eliminated with the presence of DAIs, as sketched in Fig. 4g. During Li stripping, the controlled migration of iodide anions enables the formation of a dynamic and self-adaptable interphases between the Li° anode and electrolyte (stage II in Fig. 4g). The as-formed DAIs regulate local strain and stress and homogenize internal pressure distribution (that is, 'octopus-like' behaviour), promoting close solid–solid contact between the Li° anode and electrolyte during continuous stripping (stages III and IV in Fig. 4g). Under low external pressure (<1 MPa), the DAIs enable rapid Li^+ transport across the interphases while blocking electron injection from the Li° anode, effectively preventing parasitic reactions and Li° dendrite formation (stages V and VI in Supplementary Fig. 30b). Therefore, robust DAIs circumvent voids caused by Li° anode volume contraction during stripping, ensuring close solid–solid contact, homogenizing the electric field and internal pressure distribution, preventing lithium dendrite growth and enabling long-term cycling. The impact of solid electrolyte interphase components on the working principles has also been evaluated, and the results are presented in Supplementary Discussion 9.

Discussion

Overall, the DAI strategy represents a paradigm shift in solid-state battery design, accelerating the practical implementation of high-energy and sustainable electrochemical storage systems in current energy networks. From the inherent working principle, the establishment of DAIs via controllable anion migration offers both technological sustainability and broad versatility. Specifically, anions with controllable mobility are chosen from readily available and environmentally benign elements (for example, I^-), and their preinstallation in solid electrolytes is carried out via cost-effective and scalable approaches that align well with eco-friendly, low-carbon-footprint manufacturing protocols. Moreover, beyond the iodide anions explored herein, the approach can be extended to other earth-abundant elements (for example, Br^-, Cl^-) to tailor electrolyte properties, potentially unlocking superior ionic conductivity and interfacial stability. Most importantly, the fundamental principle of DAIs is universally applicable to alkali metal anodes (Na, K), enabling the development of pressure-tolerant all-solid-state sodium/potassium batteries.

From a wider perspective, the DAI approach fundamentally resolves the critical hurdle faced by the battery industry while practicalizing ASSLMBs technology: the high stack pressure (>5 MPa) typically required to maintain solid–solid contact with prevailing ASSLMBs configurations. By reducing operational pressure to the level of current LIB technology (<1 MPa), the DAI approach eliminates the need for complex manufacturing and mechanical controlling systems while also extending the service life of ASSLMBs. This effectively mitigates battery degradation, which reduces cell maintenance and recycling burdens, thus laying a cornerstone for practical deployment of ASSLMBs in greener and more sustainable energy storage systems in the near future.

In summary, we screened potential chemical structures for anionic migration via computer simulations and experimentally verified the concept using a LiI-doped solid electrolyte. Results show that in $Li_{3.2}PS_4I_{0.2}$, long-range I^- ion migration occurs through an interstitial mechanism. Ex situ AES and in situ XPS demonstrate that the I^- ions migrate to the interface between the Li° anode and electrolyte during electrochemical cycling, achieving a DAI to maintain mechanical integrity of the interface between the Li° anode and solid electrolyte. The DAI enables stable solid–solid contact during continuous cycling, allowing Li° anode operation at 5 mAh cm^{-2} under low pressures (<1 MPa). The exemplar Li–B|$Li_{3.2}PS_4I_{0.2}$|$Li_4Ti_5O_{12}$ cell achieves 2,400 cycles, and a Li–B|$Li_{3.2}PS_4I_{0.2}$|$LiCoO_2$ pouch cell shows stable cyclability without external pressure. These intriguing findings may inspire disruptive designs for solid electrolytes with robust anode–electrolyte interphases and accelerate the development of high-energy, sustainable battery technologies employing lithium-based anodes for emerging applications.

Methods

Computational approaches

The migration ability of lithium ions and anions is evaluated by high-throughput bond-valence calculations. In this method, both the ion migration paths and energy barriers can be extracted from the energy landscape simulated by the semiempirical potentials. The crystal structures represented in crystallographic information file (cif) format are used as the input files for BV simulations.

The kinetic properties of $Li_{3.2}PS_4I_{0.2}$ are simulated by density functional theory calculations with the Vienna ab initio simulation package[58]. The exchange-correlation function of Perdew–Burke–Ernzerhof[59] is adopted. According to the experimentally determined crystal structure, the model with 0.2 LiI inserted into the crystal lattice of Li_3PS_4 to form $Li_{3.2}PS_4I_{0.2}$(Li_3PS_4·0.2LiI) is considered in the simulations. Because of the various crystal sites occupied by inserted Li^+ and I^-, 16 different configurations are relaxed via density functional theory calculations, after which the configuration with the lowest total energy is adopted to perform ab initio molecular dynamics (AIMD) to investigate the

kinetic properties of $Li_{3.2}PS_4I_{0.2}$. The structural optimizations are converged with the criteria of 10^{-5} eV and 0.01 eV $Å^{-1}$ for energy and force, respectively. Both the atom sites and the cell shape are relaxed. The cutoff energy is 520 eV, and a 2 × 2 × 3 k-mesh is used to sample the Brillouin zone. For the AIMD calculations, a Nose thermostat is adopted for the simulations with several temperatures, including 400 K, 600 K, 650 K, 700 K, 750 K, 800 K and 1,000 K. The simulations are carried out with a timestep of 1 fs and last for 110 ps. Only the gamma point is adopted for Brillouin zone sampling. The first 10 ps of the calculation is used to equilibrate the system at each temperature, and the migration pathways and transport properties of Li ions are extracted from the last 100 ps.

Electrolyte synthesis

The iodide-free (that is, Li_3PS_4) and iodide-containing (that is, $Li_{3.2}PS_4I_{0.2}$) inorganic solid electrolytes were obtained following typical solid-phase reactions. All preparation processes were carried out in an argon-filled glove box with H_2O < 0.1 ppm and O_2 < 0.1 ppm (Lab Star). To synthesize the Li_3PS_4 electrolyte, lithium sulfide (Li_2S, 99.9%, Sigma–Aldrich) and phosphorous sulfide (P_2S_5, 99%, Aladdin Chemistry Co., Ltd) were used as starting materials without pretreatment before ball milling. The starting materials for $Li_{3.2}PS_4I_{0.2}$ were Li_2S, P_2S_5 and lithium iodide (LiI, 99.9%, Aladdin Chemistry Co., Ltd). Stoichiometric starting materials were ball milled by 90-g zirconia balls (diameter of 5 mm) with a planetary ball mill apparatus (Retsch, PM400). The rotating speed and ball-milling time were 500 rpm and 15 h, respectively. For the Li_3PS_4 glass-ceramic electrolyte, the resulting mixture was annealed in alumina crucibles at 260 °C for 2 h with a heating rate of 2 °C min^{-1}. For the $Li_{3.2}PS_4I_{0.2}$ electrolyte, the resulting mixture was annealed at 220 °C for 2 h with a heating rate of 2 °C min^{-1}. After being ground with an agate mortar and pestle, homogeneous fine Li_3PS_4 and $Li_{3.2}PS_4I_{0.2}$ electrolyte powders were obtained.

Preparation of the $LiCoO_2$ cathode

The poly(methyl methacrylate-*co*-butyl acrylate) copolymer was used as a binder, and its synthesis process was reported in previous work[60]. $LiCoO_2$, Li_6PS_5Cl, vapour-grown carbon fibres and poly(methyl methacrylate-*co*-butyl acrylate) (70:30:1:3 by weight ratio) were mixed in toluene for 30 min in a dissolver (THINKY MIXER, ARE-310) to prepare a cathode slurry. Subsequently, the slurry with a solid content of 63.0 wt% was coated onto an aluminium foil substrate using an adjustable-thickness blade. After removing the toluene under 80 °C for 12 h, a cathode sheet was obtained. All preparation processes were performed in an argon-filled glove box with H_2O < 0.1 ppm and O_2 < 0.1 ppm (Lab Star).

Preparation of solid electrolyte sheets

The preparation process of sulfide electrolyte sheets involved dispersing a specific amount of solid electrolyte powder (97 wt%) and poly(methyl methacrylate-*co*-butyl acrylate) (3 wt%) in toluene with stirring to ensure the homogeneity of the resulting slurry. The obtained $Li_{3.2}PS_4I_{0.2}$ slurry with a solids content of 66.1 wt% was coated onto a polyester film followed by drying at 80 °C for 12 h. After that, a uniformly mixed Li_6PS_5Cl solid electrolyte slurry was coated onto the surface of the dried $Li_{3.2}PS_4I_{0.2}$ membrane, and a double-layer solid electrolyte sheet was prepared after removing the toluene under 80 °C for 12 h. The electrolyte sheet did not receive further treatment. The double-layer solid electrolyte sheet was employed to avoid the possible oxidation of the electrolyte at the high-voltage cathodes (Supplementary Discussion 10).

Fabrication of pouch-type full cells

Pouch-type full cells with a size of 3 cm × 3 cm were assembled to evaluate electrochemical performance. All the assembling processes were conducted in a dry argon-filled glove box (Lab Star). First, the $LiCoO_2$ cathode sheet was affixed onto the surface of the Li_6PS_5Cl solid electrolyte and subjected to isostatic pressing under 500 MPa. Then, the lithium foil was attached to the $Li_{3.2}PS_4I_{0.2}$ solid electrolyte side. The electrodes were elicited by lugs, and the whole prototype cell was encapsulated in an aluminium–plastic film. The pouch cells were evaluated with galvanostatic charge-discharge tests at 60 °C by a standard battery testing instrument (LAND CT-2001A, Wuhan Rambo Testing Equipment Co., Ltd). All the tests were cycled between 3.0 V and 4.2 V.

Preparation of the LiI-layer protected Li° anode

Li foil (99.9%, 50 µm thickness, Alfa Aesar) was polished and punched into 10-mm-diameter discs. Iodine particles (99.99%, Aladdin) were ground into powder by hand milling. The free-treated Li pieces and 2 g of iodine powder were sealed in a bottle in an argon-filled glove box with H_2O < 0.1 ppm and O_2 < 0.1 ppm. Then, the bottle was heated to 120 °C for 12 h before cooling to room temperature to obtain the final LiI layer on the Li° anode.

Characterizations

XRD tests were performed on a Bruker X-ray diffractometer (Bruker AXS D8 Advance) using Cu K_α radiation (λ = 1.5406 Å). The diffraction data were collected with a scanning step of 0.02°, a scanning speed of 12° min^{-1} and the diffractometer operating at 40 kV and 40 mA. XRD samples were measured in Ar-protected quartz cells sealed with Kapton tape (polyimide film).

Cross-section specimens were prepared using an IB-19530CP cross-section polisher (Supplementary Fig. 31), which was operated at accelerating voltages of 3–6 kV for all samples. The symmetric Li°||Li° or Li–B||Li–B cells and Li–B||$Li_4Ti_5O_{12}$ cells were disassembled in an argon atmosphere glove box (<0.1 ppm O_2 and H_2O), and then the as-formed samples were transferred to the cross polisher using an air-free holder. The samples were polished by an argon ion source under vacuum (that is, 1×10^{-4} Pa) and a low temperature (that is, −80 °C).

Field-emission SEM on a Hitachi 8100 with implemented energy-dispersive X-ray spectroscopy was used to provide information on the surface and cross section of all samples, which was operated at 5–15 kV for all samples. All samples were loaded into an air-free SEM holder within an Ar atmosphere glove box (<0.1 ppm O_2 and H_2O) and directly transported to the scanning electron microscope, where they were analysed under vacuum.

AES (JEOL JAMP-9510F) was used to examine the elements on the cross section of the interphases. An Ar ion beam from a tungsten field-emission gun with an etching rate of 0.1 nm s^{-1} was used to sputter the sample with an incidence angle of 30 ± 1° to perform AES, and the pressure during the measuring time was retained below 1×10^{-7} Pa.

In situ XPS measurements were performed in a Kratos UltraDLD photoelectron spectrometer under ultrahigh vacuum conditions, with typical base pressures below 5×10^{-10} Torr. The Al K_α X-ray monochromator was operated with an anode power of 120 W. The sample surface normal was oriented at 90° to the photoelectron spectrometer. The spectrometer pass energy was set to 20 eV. Binding energy calibrations of sputter-cleaned metal foils followed values reported by Seah for Au 4f7/2, Ag 3d5/2 and Cu 2p3/2 core levels.

In the lithium plating process of the in situ XPS experiment, an electron flood gun was used to supply electrons to the surface, and the net negative charge accumulated on the surface induced the opposite Li^+ ion migration flux. This provided a driving force for the migration of Li^+ through the $Li_{3.2}PS_4I_{0.2}$ electrolyte.

During the lithium stripping process of the in situ XPS experiment, low-energy ions were used to excite free electrons on the surface of metal lithium, that is,

$$Li^0 \rightarrow Li^+ + e^-. \quad (1)$$

Electrochemical measurements

The ionic conductivities of the electrolyte samples were characterized by the alternating current impedance method. Powder samples

(150 mg) were placed in a mould cell (10 mm in diameter) and cold pressed to pellets 10 mm in diameter at 360 MPa, and carbon plates were selected as blocking electrodes on both sides of the pellets. Electrochemical impedance spectroscopy was performed on an impedance analyser (Solartron, 1470E) at frequencies from 1 MHz to 10 Hz in an argon atmosphere.

The symmetric (that is, Li°||Li° or Li–B||Li–B) and full (that is, Li–B||$Li_4Ti_5O_{12}$) cells were assembled in an argon-filled glove box, and their cell configurations are provided in Supplementary Fig. 32. The selection of lithium and lithium–boron alloy electrodes is discussed in Supplementary Discussion 11. For symmetric cells, 150 mg of electrolyte powder (Li_3PS_4 or $Li_{3.2}PS_4I_{0.2}$) was placed in a mould cell (10 mm in diameter) and pressed under 360 MPa for 5 min. Then, Li film (50 µm, China Energy Lithium Co., Ltd) or Li–B film (60 wt% Li°, 50 µm, China Energy Lithium Co., Ltd) was placed on both sides of the electrolyte, and stainless-steel discs were introduced as current collectors by pressing under 20 MPa. For full cells, first, the electrolyte pellet (10 mm in diameter, 1,000 µm in thickness) was obtained by pressing electrolyte powder under 240 MPa (about 5 min). Second, the composite cathode powder (containing $Li_4Ti_5O_{12}$, the electrolyte and Super P, (5:4:1 by wt%); $LiCoO_2$ and the electrolyte, 7:3 by wt%; or FeS_2, the electrolyte and Super P, 4:3:1.5 by wt%) was uniformly spread on the electrolyte pellet and pressed under 240 MPa (about 5 min). Finally, the Li–B alloy foil was attached, and stainless-steel discs were introduced as current collectors by pressing under 180 MPa.

The symmetric and full cells were tested in a customized mould secured with screws. The entire process was performed in an argon-filled glove box. The tests were carried out with a standard battery test instrument (LAND CT-2001A, Wuhan Rambo Electronics Co., Ltd) at 80 °C. Alternating current impedance tests were performed on an impedance analyser (Solartron, 1470E) at frequencies from 1 MHz to 0.01 Hz in an argon atmosphere.

Control of the stack pressure applied to the solid-state cells during cycling was conducted with a special cell holder (Supplementary Fig. 20). A 200-kg load cell was mounted at the bottom of the holder along the axis of the battery, which allowed measurement of pressures between 0 MPa and 25 MPa. The bottom of the solid-state cells was in direct contact with the load cell. The stack pressure could be accurately tuned by tightening the nuts accordingly.

Reporting summary

Further information on research design is available in the Nature Research Reporting Summary linked to this article.

Data availability

The data supporting the findings of this study are available within the article and its Supplementary Information. The relevant raw data are listed in Excel documents and provided as source or Supplementary Tables 1–3. Source data are provided with this paper.

References

1. Lindley, D. The energy storage problem. *Nature* **463**, 18–20 (2010).
2. Dunn, B., Kamath, H. & Tarascon, J. M. Electrical energy storage for the grid: a battery of choices. *Science* **334**, 928–935 (2011).
3. Manthiram, A., Yu, X. W. & Wang, S. F. Lithium battery chemistries enabled by solid-state electrolytes. *Nat. Rev. Mater.* **2**, 16103 (2017).
4. Baars, J., Domenech, T., Bleischwitz, R., Melin, H. E. & Heidrich, O. Circular economy strategies for electric vehicle batteries reduce reliance on raw materials. *Nat. Sustain.* **4**, 71–79 (2020).
5. Lee, Y.-G. et al. High-energy long-cycling all-solid-state lithium metal batteries enabled by silver–carbon composite anodes. *Nat. Energy* **5**, 299–308 (2020).
6. Janek, J. & Zeier, W. G. A solid future for battery development. *Nat. Energy* **1**, 16141 (2016).
7. Bauer, C. et al. Charging sustainable batteries. *Nat. Sustain.* **5**, 176–178 (2022).
8. Schmuch, R., Wagner, R., Hörpel, G., Placke, T. & Winter, M. Performance and cost of materials for lithium-based rechargeable automotive batteries. *Nat. Energy* **3**, 267–278 (2018).
9. Kalnaus, S., Dudney, N. J., Westover, A. S., Herbert, E. & Hackney, S. Solid-state batteries: the critical role of mechanics. *Science* **381**, eabg5998 (2023).
10. Xiao, Y. et al. Understanding interface stability in solid-state batteries. *Nat. Rev. Mater.* **5**, 105–126 (2019).
11. Janek, J. & Zeier, W. G. Challenges in speeding up solid-state battery development. *Nat. Energy* **8**, 230–240 (2023).
12. Xu, L. et al. Interfaces in solid-state lithium batteries. *Joule* **2**, 1991–2015 (2018).
13. Banerjee, A., Wang, X., Fang, C., Wu, E. A. & Meng, Y. S. Interfaces and interphases in all-solid-state batteries with inorganic solid electrolytes. *Chem. Rev.* **120**, 6878–6933 (2020).
14. Chen, Y. et al. Li metal deposition and stripping in a solid-state battery via Coble creep. *Nature* **578**, 251–255 (2020).
15. Yan, H. et al. How does the creep stress regulate void formation at the lithium-solid electrolyte interface during stripping? *Adv. Energy Mater.* **12**, 2102283 (2022).
16. Kasemchainan, J. et al. Critical stripping current leads to dendrite formation on plating in lithium anode solid electrolyte cells. *Nat. Mater.* **18**, 1105–1111 (2019).
17. Lee, K., Kazyak, E., Wang, M. J., Dasgupta, N. P. & Sakamoto, J. Analyzing void formation and rewetting of thin in situ-formed Li anodes on LLZO. *Joule* **6**, 2547–2565 (2022).
18. Lewis, J. A. et al. Linking void and interphase evolution to electrochemistry in solid-state batteries using operando X-ray tomography. *Nat. Mater.* **20**, 503–510 (2021).
19. Raj, V. et al. Direct correlation between void formation and lithium dendrite growth in solid-state electrolytes with interlayers. *Nat. Mater.* **21**, 1050–1056 (2022).
20. Sun, F. et al. Visualizing the morphological and compositional evolution of the interface of InLi-anode|thio-LISION electrolyte in an all-solid-state Li–S cell by in operando synchrotron X-ray tomography and energy dispersive diffraction. *J. Mater. Chem. A* **6**, 22489–22496 (2018).
21. Wang, M. J., Choudhury, R. & Sakamoto, J. Characterizing the Li-solid-electrolyte interface dynamics as a function of stack pressure and current density. *Joule* **3**, 2165–2178 (2019).
22. Doux, J. M. et al. Stack pressure considerations for room-temperature all-solid-state lithium metal batteries. *Adv. Energy Mater.* **10**, 1903253 (2019).
23. Yan, W. et al. Hard-carbon-stabilized Li–Si anodes for high-performance all-solid-state Li-ion batteries. *Nat. Energy* **8**, 800–813 (2023).
24. Li, R. et al. Effect of external pressure and internal stress on battery performance and lifespan. *Energy Storage Mater.* **52**, 395–429 (2022).
25. Takada, K., Aotani, N., Iwamoto, K. & Kondo, S. Solid state lithium battery with oxysulfide glass. *Solid State Ion.* **86-88**, 877–882 (1996).
26. Luo, S. T. et al. Growth of lithium-indium dendrites in all-solid-state lithium-based batteries with sulfide electrolytes. *Nat. Commun.* **12**, 6968 (2021).
27. Fu, K. et al. Toward garnet electrolyte-based Li metal batteries: an ultrathin, highly effective, artificial solid-state electrolyte/metallic Li interface. *Sci. Adv.* **3**, e1601659 (2017).
28. Tan, D. H. S. et al. Carbon-free high-loading silicon anodes enabled by sulfide solid electrolytes. *Science* **373**, 1494–1499 (2021).

29. Han, S. Y. et al. Stress evolution during cycling of alloy-anode solid-state batteries. *Joule* **5**, 2450–2465 (2021).
30. Luo, W. et al. Transition from superlithiophobicity to superlithiophilicity of garnet solid-state electrolyte. *J. Am. Chem. Soc.* **138**, 12258–12262 (2016).
31. Wang, C. et al. Universal soldering of lithium and sodium alloys on various substrates for batteries. *Adv. Energy Mater.* **8**, 1701963 (2018).
32. Dubey, R. et al. Building a better Li-garnet solid electrolyte/metallic Li interface with antimony. *Adv. Energy Mater.* **11**, 2102086 (2021).
33. Han, X. et al. Negating interfacial impedance in garnet-based solid-state Li metal batteries. *Nat. Mater.* **16**, 572–579 (2017).
34. Lu, Y. et al. Highly stable garnet solid electrolyte based Li-S battery with modified anodic and cathodic interfaces. *Energy Storage Mater.* **15**, 282–290 (2018).
35. Visco, S. J. & Tsang, F. Y. Method for forming encapsulated lithium electrodes having glass protective layers. US Patent 6,214,061 (2001).
36. Fan, X. et al. Fluorinated solid electrolyte interphase enables highly reversible solid-state Li metal battery. *Sci. Adv.* **4**, eaau9245 (2018).
37. Lu, Y., Tu, Z. & Archer, L. A. Stable lithium electrodeposition in liquid and nanoporous solid electrolytes. *Nat. Mater.* **13**, 961–969 (2014).
38. Krauskopf, T., Richter, F. H., Zeier, W. G. & Janek, J. Physicochemical concepts of the lithium metal anode in solid-state batteries. *Chem. Rev.* **120**, 7745–7794 (2020).
39. Zhao, Q., Stalin, S., Zhao, C. Z. & Archer, L. A. Designing solid-state electrolytes for safe, energy-dense batteries. *Nat. Rev. Mater.* **5**, 229–252 (2020).
40. Bachman, J. C. et al. Inorganic solid-state electrolytes for lithium batteries: mechanisms and properties governing ion conduction. *Chem. Rev.* **116**, 140–162 (2016).
41. Xiao, R., Li, H. & Chen, L. High-throughput design and optimization of fast lithium ion conductors by the combination of bond-valence method and density functional theory. *Sci. Rep.* **5**, 14227 (2015).
42. Wu, S., Xiao, R., Li, H. & Chen, L. New insights into the mechanism of cation migration induced by cation–anion dynamic coupling in superionic conductors. *J. Mater. Chem. A* **10**, 3093–3101 (2022).
43. Liu, X. et al. Local electronic structure variation resulting in Li `filament' formation within solid electrolytes. *Nat. Mater.* **20**, 1485–1490 (2021).
44. Han, F. D., Yue, J., Zhu, X. Y. & Wang, C. S. Suppressing Li dendrite formation in Li2S-P2S5 solid electrolyte by LiI incorporation. *Adv. Energy Mater.* **8**, 1703644 (2018).
45. Zhu, L. et al. Enhancing ionic conductivity in solid electrolyte by relocating diffusion ions to under-coordination sites. *Sci. Adv.* **8**, eabj7698 (2022).
46. Huang, J. et al. Deep potential generation scheme and simulation protocol for the $Li_{10}GeP_2S_{12}$-type superionic conductors. *J. Chem. Phys.* **154**, 094703 (2021).
47. Zhang, Z. & Nazar, L. F. Exploiting the paddle-wheel mechanism for the design of fast ion conductors. *Nat. Rev. Mater.* **7**, 389–405 (2022).
48. Ujiie, S., Hayashi, A. & Tatsumisago, M. Structure, ionic conductivity and electrochemical stability of Li_2S–P_2S_5–LiI glass and glass–ceramic electrolytes. *Solid State Ion.* **211**, 42–45 (2012).
49. Rangasamy, E. et al. An iodide-based $Li_7P_2S_8I$ superionic conductor. *J. Am. Chem. Soc.* **137**, 1384–1387 (2015).
50. Qing, P. et al. Highly reversible lithium metal anode enabled by 3D lithiophilic–lithiophobic dual-skeletons. *Adv. Mater.* **35**, 2211203 (2023).
51. Zhang, X. X. et al. Topology fortified anodes powered high-energy all-solid-state lithium batteries. *Adv. Mater.* **37**, 2506298 (2025).
52. Wood, K. N. et al. Operando X-ray photoelectron spectroscopy of solid electrolyte interphase formation and evolution in Li_2S-P_2S_5 solid-state electrolytes. *Nat. Commun.* **9**, 2490 (2018).
53. Zaghib, K., Simoneau, M., Armand, M. & Gauthier, M. Electrochemical study of $Li_4Ti_5O_{12}$ as negative electrode for Li-ion polymer rechargeable batteries. *J. Power Sources* **81–82**, 300–305 (1999).
54. Zuo, T.-T. et al. A mechanistic investigation of the $Li_{10}GeP_2S_{12}$|$LiNi_{1-x-y}Co_xMn_yO_2$ interface stability in all-solid-state lithium batteries. *Nat. Commun.* **12**, 6669 (2021).
55. Shi, T. et al. Characterization of mechanical degradation in an all-solid-state battery cathode. *J. Mater. Chem. A* **8**, 17399–17404 (2020).
56. Tan, D. H. S., Meng, Y. S. & Jang, J. Scaling up high-energy-density sulfidic solid-state batteries: a lab-to-pilot perspective. *Joule* **6**, 1755–1769 (2022).
57. Ning, Z. et al. Dendrite initiation and propagation in lithium metal solid-state batteries. *Nature* **618**, 287–293 (2023).
58. Kresse, G. & Furthmuller, J. Efficient iterative schemes for ab initio total-energy calculations using a plane-wave basis set. *Phys. Rev. B* **54**, 11169–11186 (1996).
59. Perdew, J. P., Burke, K. & Ernzerhof, M. Generalized gradient approximation made simple. *Phys. Rev. Lett.* **77**, 3865–3868 (1996).
60. Urban, M. W. et al. Key-and-lock commodity self-healing copolymers. *Science* **362**, 220–225 (2018).
61. Yang, C. et al. Continuous plating/stripping behavior of solid-state lithium metal anode in a 3D ion-conductive framework. *Proc. Natl Acad. Sci. USA* **115**, 3770–3775 (2018).
62. Wan, J. et al. Ultrathin, flexible, solid polymer composite electrolyte enabled with aligned nanoporous host for lithium batteries. *Nat. Nanotechnol.* **14**, 705–711 (2019).
63. Zhao, Q., Liu, X., Stalin, S., Khan, K. & Archer, L. A. Solid-state polymer electrolytes with in-built fast interfacial transport for secondary lithium batteries. *Nat. Energy* **4**, 365–373 (2019).
64. Wang, K. et al. A cost-effective and humidity-tolerant chloride solid electrolyte for lithium batteries. *Nat. Commun.* **12**, 4410 (2021).
65. Choudhury, S. et al. Solid-state polymer electrolytes for high-performance lithium metal batteries. *Nat. Commun.* **10**, 4398 (2019).
66. Yin, Y. C. et al. A $LaCl_3$-based lithium superionic conductor compatible with lithium metal. *Nature* **616**, 77–83 (2023).
67. Ye, L. & Li, X. A dynamic stability design strategy for lithium metal solid state batteries. *Nature* **593**, 218–222 (2021).
68. Shi, P. et al. A dielectric electrolyte composite with high lithium-ion conductivity for high-voltage solid-state lithium metal batteries. *Nat. Nanotechnol.* **18**, 602–610 (2023).
69. Zhang, W., Nie, J., Li, F., Wang, Z. L. & Sun, C. A durable and safe solid-state lithium battery with a hybrid electrolyte membrane. *Nano Energy* **45**, 413–419 (2018).
70. Chena, L. et al. PEO/garnet composite electrolytes for solid-state lithium batteries: from 'ceramic-in-polymer' to 'polymer-in-ceramic'. *Nano Energy* **46**, 176–184 (2017).
71. Xu, B. et al. Interfacial chemistry enables stable cycling of all-solid-state Li metal batteries at high current densities. *J. Am. Chem. Soc.* **143**, 6542–6550 (2021).
72. Qiao, L. et al. Trifluoromethyl-free anion for highly stable lithium metal polymer batteries. *Energy Storage Mater.* **32**, 225–233 (2020).
73. Hu, J., He, P., Zhang, B., Wang, B. & Fan, L.-Z. Porous film host-derived 3D composite polymer electrolyte for high-voltage solid state lithium batteries. *Energy Storage Mater.* **26**, 283–289 (2020).

74. Duan, H. et al. Extended electrochemical window of solid electrolytes via heterogeneous multilayered structure for high-voltage lithium metal batteries. *Adv. Mater.* **31**, 1807789 (2019).
75. Liang, H. et al. Polysiloxane-based single-ion conducting polymer blend electrolyte comprising small-molecule organic carbonates for high-energy and high-power lithium-metal batteries. *Adv. Energy Mater.* **12**, 2200013 (2022).
76. Huo, H. et al. Rational design of hierarchical 'ceramic-in-polymer' and 'polymer-in-ceramic' electrolytes for dendrite-free solid-state batteries. *Adv. Energy Mater.* **9**, 1804004 (2019).
77. Wang, H. et al. Thiol-branched solid polymer electrolyte featuring high strength, toughness, and lithium ionic conductivity for lithium-metal batteries. *Adv. Mater.* **32**, e2001259 (2020).

Acknowledgements

X.Y. acknowledges support from the National Key R&D Program of China (grant no. 2022YFB3807700), National Natural Science Foundation of China (grant no. 52372244) and Youth Innovation Promotion Association, Chinese Academy of Sciences (CAS) (grant no. Y2021080). H.Y. acknowledges support from the Youth Innovation Promotion Association, CAS (grant no. 2023009). L.B. acknowledges support from the National Natural Science Foundation of China (grant no. 22179144). R.X. acknowledges support from the Strategic Priority Research Program of CAS (grant no. XDB1040302). G.L. acknowledges support from the National Natural Science Foundation of China (grant no. 22309194).

Author contributions

X.H. conceived the original idea. X.H., H.Z. and X.Y. directed the work. H.Y. and G.C. designed the experiments. G.C., R.Q., J.Z., X.Z., G.L. and K.J. carried out the experiments and measurements. R.X. conducted the simulations. H.Y. and L.B. assisted with characterization. G.C., X.H., H.Z. and X.Y. wrote the initial draft, and all authors contributed to the writing of the final manuscript.

Competing interests

The authors declare no competing interests.

Additional information

Supplementary information The online version contains supplementary material available at https://doi.org/10.1038/s41893-025-01649-y.

Correspondence and requests for materials should be addressed to Xiayin Yao, Heng Zhang or Xuejie Huang.

Peer review information *Nature Sustainability* thanks the anonymous reviewers for their contribution to the peer review of this work.

nature portfolio

Corresponding author(s): Xuejie Huang

Last updated by author(s): May 14, 2025

Reporting Summary

Nature Portfolio wishes to improve the reproducibility of the work that we publish. This form provides structure for consistency and transparency in reporting. For further information on Nature Portfolio policies, see our Editorial Policies and the Editorial Policy Checklist.

Statistics

For all statistical analyses, confirm that the following items are present in the figure legend, table legend, main text, or Methods section.

n/a	Confirmed
☒	☐ The exact sample size (*n*) for each experimental group/condition, given as a discrete number and unit of measurement
☒	☐ A statement on whether measurements were taken from distinct samples or whether the same sample was measured repeatedly
☒	☐ The statistical test(s) used AND whether they are one- or two-sided *Only common tests should be described solely by name; describe more complex techniques in the Methods section.*
☒	☐ A description of all covariates tested
☒	☐ A description of any assumptions or corrections, such as tests of normality and adjustment for multiple comparisons
☒	☐ A full description of the statistical parameters including central tendency (e.g. means) or other basic estimates (e.g. regression coefficient) AND variation (e.g. standard deviation) or associated estimates of uncertainty (e.g. confidence intervals)
☒	☐ For null hypothesis testing, the test statistic (e.g. *F*, *t*, *r*) with confidence intervals, effect sizes, degrees of freedom and *P* value noted *Give P values as exact values whenever suitable.*
☒	☐ For Bayesian analysis, information on the choice of priors and Markov chain Monte Carlo settings
☒	☐ For hierarchical and complex designs, identification of the appropriate level for tests and full reporting of outcomes
☒	☐ Estimates of effect sizes (e.g. Cohen's *d*, Pearson's *r*), indicating how they were calculated

Our web collection on statistics for biologists contains articles on many of the points above.

Software and code

Policy information about availability of computer code

Data collection	LANDdt(v5.9); Solartron 1470E; Gaussian16 package; SEM, Hitachi S-4800; XRD, Bruker AXS D8 Advance; AES, JEOL JAMP-9510F; AES, Kratos UltraDLD
Data analysis	Vesta; Origin; Zview

For manuscripts utilizing custom algorithms or software that are central to the research but not yet described in published literature, software must be made available to editors and reviewers. We strongly encourage code deposition in a community repository (e.g. GitHub). See the Nature Portfolio guidelines for submitting code & software for further information.

Data

Policy information about availability of data

All manuscripts must include a data availability statement. This statement should provide the following information, where applicable:

- Accession codes, unique identifiers, or web links for publicly available datasets
- A description of any restrictions on data availability
- For clinical datasets or third party data, please ensure that the statement adheres to our policy

The data supporting the findings of this study are available within the article and its Supplementary Information files. The relevant raw data are listed in Excel documents and provided as source or supplementary data files.

Research involving human participants, their data, or biological material

Policy information about studies with human participants or human data. See also policy information about sex, gender (identity/presentation), and sexual orientation and race, ethnicity and racism.

Reporting on sex and gender	Not relevant
Reporting on race, ethnicity, or other socially relevant groupings	Not relevant
Population characteristics	Not relevant
Recruitment	Not relevant
Ethics oversight	Not relevant

Note that full information on the approval of the study protocol must also be provided in the manuscript.

Field-specific reporting

Please select the one below that is the best fit for your research. If you are not sure, read the appropriate sections before making your selection.

☐ Life sciences ☐ Behavioural & social sciences ☒ Ecological, evolutionary & environmental sciences

For a reference copy of the document with all sections, see nature.com/documents/nr-reporting-summary-flat.pdf

Ecological, evolutionary & environmental sciences study design

All studies must disclose on these points even when the disclosure is negative.

Study description	The combination of high energy density and sustainability makes ASSLMBs a technology of growing importance. However, the challenge of void formation at interfaces causes performance degradation. Here the authors show a designer dynamic conformal interphase that adaptes to anode volume changes, achieving remarkable stability with zero external pressure in pouch cells.
Research sample	N/A
Sampling strategy	N/A
Data collection	The raw data were obtained from the experiments and recorded by experimental instruments.
Timing and spatial scale	N/A
Data exclusions	N/A
Reproducibility	See Methods.
Randomization	N/A
Blinding	N/A

Did the study involve field work? ☐ Yes ☒ No

Reporting for specific materials, systems and methods

We require information from authors about some types of materials, experimental systems and methods used in many studies. Here, indicate whether each material, system or method listed is relevant to your study. If you are not sure if a list item applies to your research, read the appropriate section before selecting a response.

Materials & experimental systems

n/a	Involved in the study
☒	☐ Antibodies
☒	☐ Eukaryotic cell lines
☒	☐ Palaeontology and archaeology
☒	☐ Animals and other organisms
☒	☐ Clinical data
☒	☐ Dual use research of concern
☒	☐ Plants

Methods

n/a	Involved in the study
☒	☐ ChIP-seq
☒	☐ Flow cytometry
☒	☐ MRI-based neuroimaging

Plants

Seed stocks	N/A
Novel plant genotypes	N/A
Authentication	N/A